

ROCK FABRIC AND TEXTURE FROM DIGITAL CORE ANALYSIS

M. Saadatfar¹, M. L. Turner¹, C. H. Arns¹, H. Averdunk¹, T.J. Senden¹, A. P. Sheppard¹, R. M. Sok^{1,2}, W. V. Pinczewski², J. Kelly³ and M.A. Knackstedt^{1,2,*}

¹Department of Applied Mathematics, Research School of Physical Sciences and Engineering, Australian National University, Canberra, Australia

²School of Petroleum Engineering, University of New South Wales, Sydney, Australia

³Woodside Energy, Perth, Western Australia

*Corresponding Author: mark.knackstedt@anu.edu.au

Copyright 2005, held jointly by the Society of Petrophysicists and Well Log Analysts (SPWLA) and the submitting authors.

This paper was prepared for presentation at the SPWLA 46th Annual Logging Symposium held in New Orleans, Louisiana, United States, June 26-29, 2005.

ABSTRACT

Descriptions of rock fabric and texture are of great value to geologists and petrophysicists as they can be used in facies analysis and in the interpretation of the environment of deposition. Grain shape and size information is used to correlate to petrophysical properties. They are also of importance to the production technologist for completion design and sand strength/failure prediction. Textural descriptions are traditionally obtained via petrographic and petrological analysis including thin section analysis, particle sieving techniques and laser diffraction studies. All methods have limitations in quantitatively describing the full 3D rock fabric and assumptions and interpretations in the processing of data can skew or distort predictions of textural data.

We have previously demonstrated the ability to image, visualize and characterise sedimentary rock in three dimensions (3D) at the pore/grain scale via X-ray computed microtomography [1, 2]. We now demonstrate the ability to directly measure rock fabric and texture from 3D digital images of core fragments. The mathematical procedure to extract individual particles from a full core image is described and its accuracy demonstrated. A single core fragment image can yield more than 8,000 individual grains. We describe methods for mathematically characterizing the individual grains including grain size (max/min and mode, skewness, sorting, kurtosis) and shape (sphericity, roundness). These are measured in parallel with textural information (sorting, grain contacts, matrix/grain support).

A comparison of grain size analysis from digital image data to laser diffraction studies on sister core material is shown; good agreement between estimates of grain size is obtained. Comprehensive grain shape data obtained over thousands of grains shows significant vari-

ability within samples and systematic shape changes with grain size. Measures of grain contacts and grain overlap area show that many grains are loose within the pack and larger grains can have coordination numbers greater than 20. Anisotropy in grain orientation is also directly measured.

The rock fabric and texture derived from digital 3D images is more comprehensive, systematic and quantitative than current analysis techniques. This analysis, coupled with studies of 3D pore structure and the ability to directly measure petrophysical properties from 3D images, will enable one to embark on a systematic study of the effect of grain size, shape and cementation on transport and elastic properties of core material.

METHODOLOGY

In this section we describe the samples considered in this study; a simple polymeric foam structure, two soil samples, a poorly consolidated reservoir core and a poorly sorted reservoir sand. We briefly describe the methods used to image the 3D structure of the porous samples and to identify the distinct phases. We discuss the computational methods used to extract individual grains from three dimensional images and discuss the mathematical tools used to analyse the size and shape of the extracted grains and the fabric of the samples.

Tomographic Imaging

A high-resolution and large-field X-ray μ CT facility has been used [17, 18, 19] to image the samples. The CT has a cone beam geometry. Details of the equipment and experimental methodology used to image the microstructure of sedimentary rock have been given previously [18, 10, 2]. The resolution chosen is dependent on the grain size of the material. For grains of 100 – 300 μ m we find that 4-10 μ m resolution is sufficient.



Figure 1: A core sample of 7.5mm x 7.5mm cross section mounted on the tomography rotation stage before imaging.

Samples imaged

Five samples are considered in this study. Details of the image size and image resolution for each of the samples is given in Table 1.

1. A microcellular polymeric foam was chosen as a *model* system for study. The foam is characterised by reasonably homogeneous spherical pores embedded within a solid matrix. This system of highly spherical and rounded pores is used to validate the fabric and texture analysis algorithms and to illustrate reference values for a sphere pack. Slices through the sample and a 3D rendered image showing the spherical structure of the foams are given in Fig 2(a) and Fig. 3(a).
2. Two samples (Soil A and B) of unconsolidated regolith material from the saturated zone (depth=50.5m) are considered. The samples come from a fairly extensive facies that appears homogenous on a cm scale. XRD analysis shows that the mineral phase is made up of 88% quartz, 9% montmorillonite and 3% kaolin. A PQ diamond coring technique was used to remove the material from the ground in a reasonably undisturbed state. Imaged slices of the samples are shown in Fig 2(b) and (c) with an aluminium tube of diameter 1.5 cm surrounding the core (left image). We note that the cut of soil A seems to contain larger grains with some layers exhibiting finer grains (Fig 2(b) right). A 3D rendered image of a small subset of Soil A is shown in Fig 3(b).
3. A sample of unconsolidated core from a prospective oil reservoir was considered. Slices of the sample are shown in Fig 2(d). A 3D rendered image of a small subset of this sample is shown in Fig 3(c).
4. A single 8 mm diameter plug of a texturally complex sample from a prospective gas reservoir was examined. The sample exhibited extremely poor

sorting and some clay content. Orthogonal slices through the original tomogram are shown in Fig. 2(e).

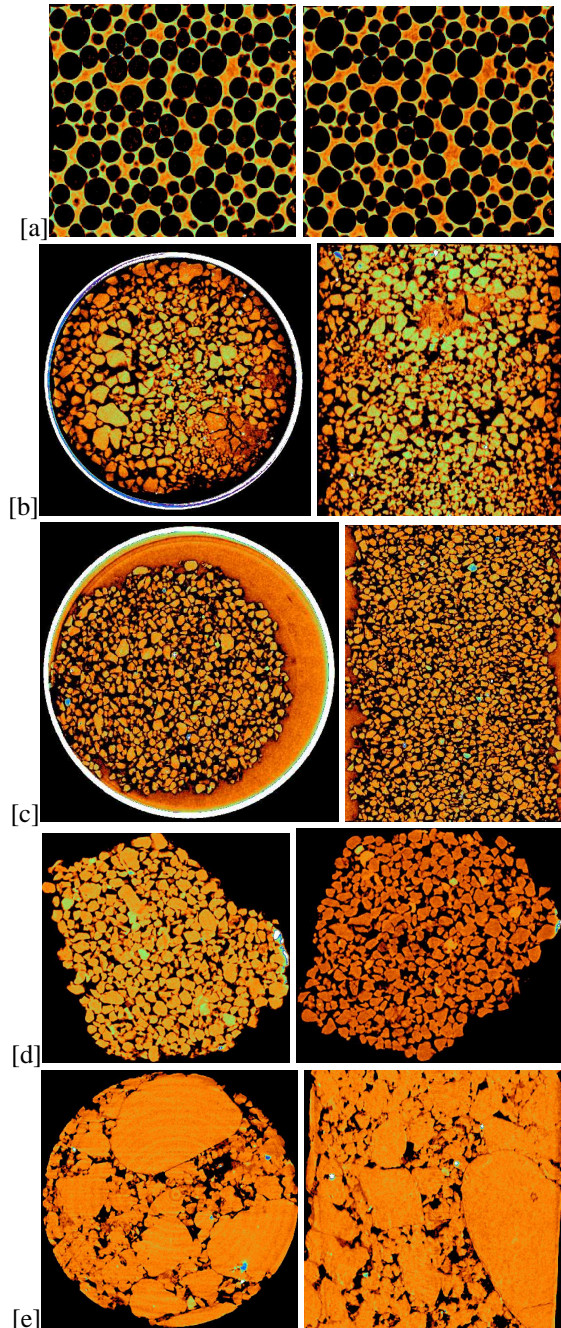


Figure 2: Orthogonal slices of the five samples imaged. (a) Foam, (b) Soil A, (c) Soil B, (d) unconsolidated sand and (e) poorly sorted sand. The phase surrounding the granular core in (c) is an injected epoxy resin.

Table 1: Details of the sample type, tomogram resolution (μm), image size (voxels), grain phase fraction ϕ_{gr} , porosity ϕ and clay/silt fraction $\phi_{s/c}$ for the samples considered in this study.

Sample	Res.	Size	ϕ_{gr}	ϕ	$\phi_{s/c}$
Foam	6.72	1000 ³	72%	28%	0%
Soil 1	17.0	1000 ³	58%	8%	34%
Soil 2	9.4	2000 ³	62%	9%	29%
Uncon.	6.72	1000 ³	70.8%	29.2%	0%
Poor Sort	8.6	1000 ³	78.4%	7.2%	14.4%

Phase Identification

The tomographic image consists of a cubic array of reconstructed linear x-ray attenuation coefficient values, each corresponding to a finite volume cube (voxel) of the sample. An immediate goal is to differentiate the attenuation map into distinct pore and grain phases for each of the samples imaged. Ideally one would wish to have a multimodal distribution giving unambiguous phase separation of the pore and various mineral phase peaks. In particular one would like to obtain a clear bimodal distribution separating the pore phase from mineral phase peaks. This simple phase extraction is possible on the polymeric foam sample. From the original 1000³ image we extract a $456 \times 456 \times 912$ subset (the region of the image which contains only foam) for analysis. The intensity histogram (Fig. 4(a)) shows two distinct peaks associated with the two phases. The peak centered around 27500 is associated with the polymeric material. The lower peak around 17000 is associated with the pore phase. For an intensity histogram with two distinct phase peaks it is sufficient to do a simple threshold segmentation at 22500 followed by an isolated cluster removal to remove noise artifacts (isolated phase fragments of ≤ 20 voxels). Comparison of the grey-scale and binarised image of a slice of foam A is shown in Fig. 4(b) and (c). The resultant solid phase fraction at the measured attenuation cutoff is $(\rho/\rho_s)_{image} = 28\%$. This is in good agreement with the lab measured density of 29%.

Unfortunately in rock and soil samples, the presence of pores at scales below the image resolution leads to a spread in the low density signal making it difficult to *unambiguously* differentiate the pore from the microporous and solid mineral phases. One also may wish to undertake three-phase identification—phase separation of the resolvable pore phase, intermediate (silt/clay) phase and the grain phase. To quantitatively analyse tomograms we have developed a well-defined and consistent method to label each voxel [20]. The first stage comprises a nonlinear anisotropic diffusion (AD) filter [13] which removes

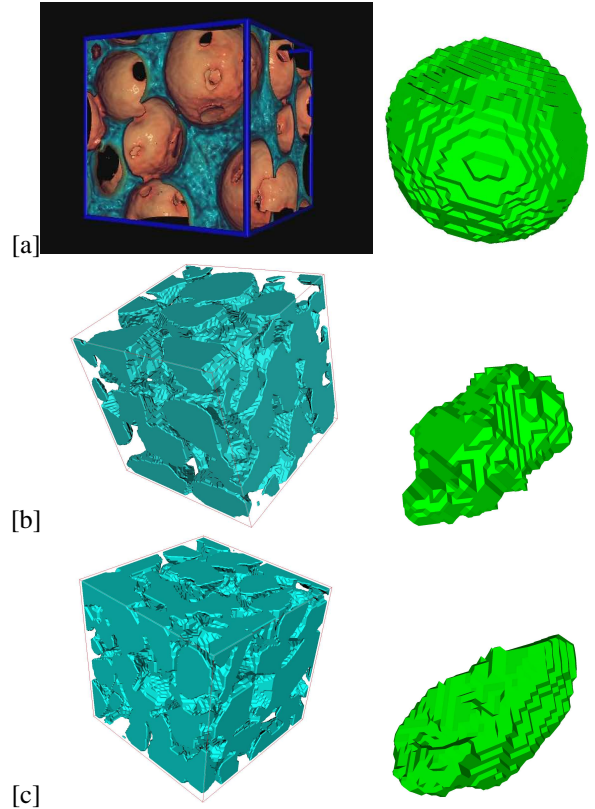


Figure 3: Rendered 3D images of subsets of samples imaged (left) and a typical grain (right). (a) Foam, (b) Soil A, (c) unconsolidated sand.

noise while preserving significant features, i.e. the boundary regions between the phases. The second stage applies an unsharp mask (UM) sharpening filter [15] which has proven itself in practice to be highly effective at sharpening edges without overly exaggerating the noise. Finally, the phase separation is performed using a combination of watershed [23] and active contour methods [3].

We describe the multiphase identification process for Soil

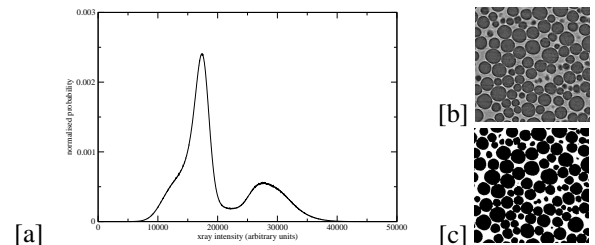


Figure 4: (a) Intensity histogram for the full image volume of Sample A. (b) Grey-scale x-ray density map of a slice of Sample A, and (c) the same slice after phase separation into pore and solid phases.

B. From the original 2000^3 of the soil sample shown in Fig. 2(c) we extract a $1080 \times 1050 \times 1900$ subset (the region of the image which contains only the sample) for phase separation. The intensity histogram for the region is given in Fig. 5 after filtering. Three phase segmenta-

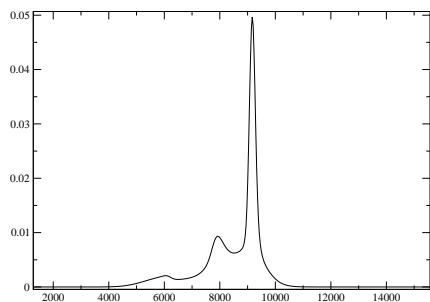


Figure 5: Normalized intensity histogram for the full image volume of the Soil B sample.

tion was performed on the image. Absolute thresholds were chosen for the void phase $I < 6500$, grain phase $I > 9000$ and intermediate (clay/silt) phase $7000 < I < 8500$. Phase separation in the ambiguous intensity regions between these phases was then made using the active contours and watershed methods to delineate the three phases. A subset of the central slice along with the resultant pore, clay and grain phases are shown in Fig. 6. The resultant phase fractions obtained were $\phi_{pore} = 9.4\%$, $\phi_{grain} = 61.7\%$, $\phi_{clay/silt} = 28.7\%$. In the other soil sample and the poorly sorted sand we undertake this three phase segmentation process and observe a significant clay fraction (Table 1). The unconsolidated sand is clean and exhibits only trace amounts of an intermediate phase.

GRAIN EXTRACTION

In sedimentary rocks the solid phase is made up of distinct grains and cements. However, due to the process of sedimentation and diagenesis the solid phase will appear continuous within the image as all grains are in contact with at least three other grains. One must develop an automated method to distinguish between particles in an image. In this section we describe two methods we use to extract distinct grains from the mineral phase of 3D tomographic images. Both methods are based on introducing grain boundaries at minima of a distance function for the grain phase. For poorly cemented sands the method is robust. For more strongly cemented materials (particularly quartz sands with quartz cement) the partitioning is more difficult and will need to be rigorously tested.

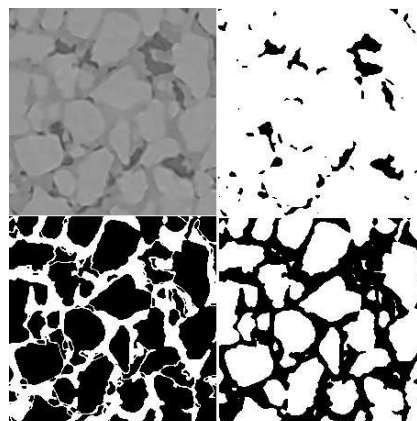


Figure 6: (Top left), Tomographic grey scale data: Top right, pore phase (black): Bottom left, clay phase (in white) and bottom right grain phase (white)

Partitioning via Erosion and Voronoi tessellation

The first algorithm is based on an erosion/dilation process followed by a voronoi partitioning—the method is illustrated in Fig. 7 for both a 2D and 3D sample. In this algorithm the grain phase image in Fig. 7(a)-(b) is first eroded which breaks apart the individual grains (Fig. 7(c)-(d)). During the erosion process we monitor the number of distinct grains until a maximum is reached. On reaching this maximum we assume that the grain phase is now broken up into all original distinct grains. Each grain is identified and the original grain shape restored by performing a dilation (opposite of erosion) back to the original image. After defining the separate particles, we now partition the space using the Voronoi tessellation so that each Voronoi cell contains a rock grain (Fig. 7(e)-(f)). A Voronoi region associated with a feature is a set of points closer to that feature than any other features. The Voronoi cells are first defined by the center of mass of each identified grain (Voronoi seed) and then by growing the Voronoi seeds at the same rate via dilation. When the boundary of two growing seeds meet a planar boundary is defined between them. The process continues until all the grain phase is filled. The Voronoi regions associated with each grain (Voronoi cells) are convex polyhedra in 3D (Fig. 7(e)-(f)) and the boundary between two adjacent cells is a plane which defines the overlap between the two distinct grains. The final grain configuration for the original image shown in Fig. 7(a)-(b) is shown in Fig. 7(g)-(h))

Partitioning via Watershed Algorithm

The first algorithm performs well, but can lead to the loss of the smallest grains during the erosion process. A second algorithm overcomes this limitation; grain identifi-

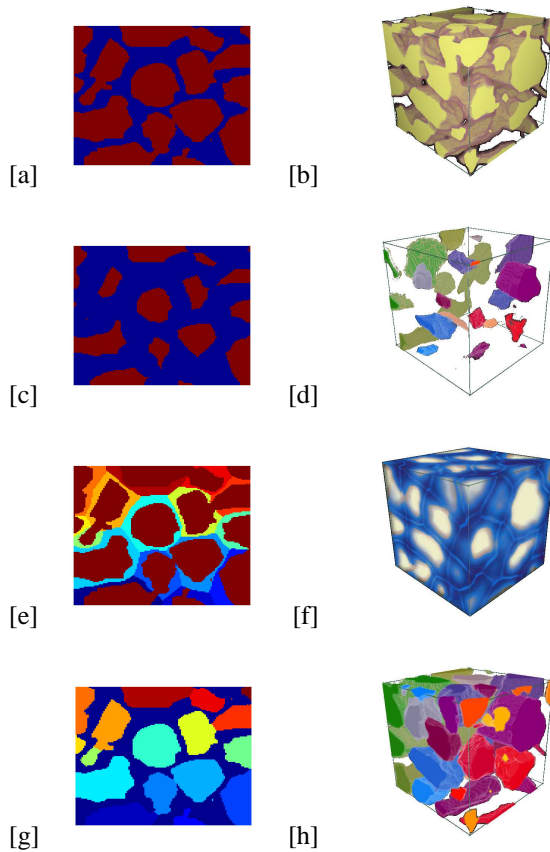


Figure 7: (a-b) A segmented image of a grain pack in (a) 2D and (b) 3D. (c-d) Images (a-b) after erosion. (e-f) shows the original images after separating the constituent grains via the Voronoi tessellation and (e) shows the boundaries separating the distinct grains in (a). (g-h) shows the original grain pack with colours labelling the distinct grains.

ation is done in a two stage process, which takes Euclidean distance data (distance to the nearest grain boundary) of the grain phase as input. The basic assumption is that the boundaries between grains which are not isolated coincide with the watershed surfaces of the Euclidean distance function [23]. The entire grain space can be thought of as the union of spheres centred on every grain voxel. Each sphere radius is given by the Euclidean distance value of the voxel at its centre. We first identify all the voxels that are not covered by any larger Euclidean spheres. Each one of these voxels, which are at maxima of the distance function in their local neighbourhood, forms a seed that will grow into a single grain in the next stage of the algorithm.

The watershed transformation [7] is performed by region growing, in which each region starts as a single seed voxel.

Voxels that lie on the boundaries of the regions are processed in reverse Euclidean distance order, i.e. voxels with high distance values are processed first. When a voxel is processed, it is assigned to the region on whose boundary it lies, or, if it lies on more than one region boundary, the region whose boundary it first became part of. At the end of the algorithm, the grain space will be partitioned into grains whose boundaries lie on the watershed surfaces of the Euclidean distance function. The algorithm is parallelised using an implementation of the "time warp" discrete event simulation protocol [22]. The resultant grain separation is nearly identical to the Voronoi based partitioning, but includes more information on smaller grains.

GRAIN SIZE, SHAPE AND TEXTURE

The granular image is now separated into distinct grains which are stored in a simple database with information on the coordinates of each grain center of mass, the coordinates of all voxels of each grain, the number of neighbouring grains and all neighboring grain labels along with grain overlap information. From the individual grain data a number of grain size, shape, texture and fabric properties can be derived.

Grain Size distribution

From the set of individual grains identified one can immediately define a comprehensive sediment size distribution and distribution measures including median and mean grain size, sorting, skewness and kurtosis. The grain volume is measured by counting the voxels in each distinct grain. Size according to the Wentworth grade scale is reported. In this grading scale one considers a logarithmic grading [11] based on:

$$\phi_g = -\log_2 d, \quad (1)$$

where d is the particle size in mm . Here we define size via the volume of the particle and report the nominal diameter d of the sphere having the same volume as the particle. Grain size distribution descriptors for each sample are defined according to Folk and Ward [6]:

$$\begin{aligned} \bar{\phi}_g &= \frac{\phi_{g16} + \phi_{g50} + \phi_{g84}}{3}, \\ Md_{\phi_g} &= \phi_{g50}, \\ \sigma &= \frac{\phi_{g84} - \phi_{g16}}{4} + \frac{\phi_{g95} - \phi_{g5}}{6.6}, \\ Sk &= \frac{\phi_{g84} + \phi_{g16} - 2\phi_{g50}}{2(\phi_{g84} - \phi_{g16})} + \frac{\phi_{g95} + \phi_{g5} - 2\phi_{g50}}{2(\phi_{g95} - \phi_{g5})}, \\ K &= \frac{\phi_{g95} - \phi_{g5}}{2.44(\phi_{g75} - \phi_{g25})}, \end{aligned}$$

where $\bar{\phi}_g$ is the mean of the grain size distribution, Md_{ϕ_g} its median, sorting is given by the standard deviation σ , Sk and K are Skewness and Kurtosis, and ϕ_{g_n} indicates the n^{th} percentile of ϕ_g .

Grain Shape derived from Spherical Harmonics

In this section we discuss how to mathematically characterize the shape of any arbitrary particle and we apply this mathematical description to the particles extracted from the 3D images. Unfortunately the discrete or voxelated representation of particles leads to significant errors in any calculation related to the surface of the particle due to the roughness of a voxelated surface. For example the digital surface area of a sphere is 50% larger than the actual value. Work on a range of oblate and prolate spheroids [8] shows the error can vary from 28% to 43%. The procedure we use to more accurately generate the 2D surface of each 3D particle is based on spherical harmonic shape descriptors of the grain surface. This method has been previously used to approximate molecular orbital surfaces [5], to characterize the shape of an asteroid [28] and to estimate the shape of cement particles [8] from digital images.

To approximate the rough surface of a voxelated object to a continuous and smooth surface via spherical harmonics we first determine the position of all the surface points in terms of polar coordinates. This is done by finding the center of mass (C_m) of the object and the line segments (R) starting from the C_m and ending at the interface between the particle (solid phase) and the background (pore phase), at all given spherical polar coordinate angles (θ and ϕ). The angles are chosen based on 120-point Gaussian quadrature [16]. This method of finding the surface points works only for particles in which the line segment connecting the center of mass to the surface crosses the interface only once; the grain is convex. The function $R(\theta, \phi)$, the spherical harmonics form a complete set:

$$r(\theta, \phi) = \sum_{n=0}^{\infty} \sum_{m=-n}^n a_{nm} Y_n^m(\theta, \phi); \quad -n \leq m \leq n \quad (2)$$

where $Y_n^m(\theta, \phi)$ is a spherical harmonic function of order (n,m) and (a_{nm}) are the Fourier coefficients. The accuracy of spherical harmonic analysis with respect to the number of coefficients n used in the spherical harmonic expansion, has been previously studied in [8]. Depending on the resolution of the digital image, different n are needed to estimate the shape properties of the object within a reasonable agreement with the exact (analytical) results. We have found, in agreement with [8], that for grains of more than 1000 voxels, the error in the estimation of the granular shape is low for $n \approx 20$. This was tested on a range of analytic shapes. For example,

error analysis on ellipsoids of revolution of 20000 voxels led to a decrease in the error in the surface area from 28% (voxel-based) to 2% (spherical harmonics, $n = 20$). From this description of the grain we can more accurately quantify sphericity and roundness.

Sphericity

Sphericity measures the degree to which a particle approaches a spherical shape. Quantitatively, sphericity was defined by Wadell [24] as the ratio of the particle's volume to the volume of a circumscribing sphere which may be taken as the volume of a sphere with a diameter equal to the longest axis of the particle;

$$\Psi_W = \sqrt[3]{\frac{V_p}{V_{cs}}} \quad (3)$$

A more accurate definition of sphericity involves measuring the three linear dimensions of the grains. From measurement of volume, surface area and curvature of each grain we derive an equivalent regular triaxial ellipsoid with Long, Intermediate and Small axes d_L and d_I and d_S respectively. Sphericity is then rewritten as;

$$\Psi = \sqrt[3]{\frac{d_S d_I}{d_L^2}} \quad (4)$$

This definition is known as *intercept sphericity*. Sneed and Folk [21] introduced *maximum projection sphericity* as a modification to Wadell's definition. Their objection to Wadell's sphericity was that although it correctly measures the degree to which a particle approaches a sphere, it does not correctly express the dynamic behavior of the particle in a fluid. They believed that the sphericity of a particle should express its behavior in a fluid where particles tend to orient themselves with their maximum projection area normal to the flow. They defined sphericity as;

$$\Psi_P = \sqrt[3]{\frac{d_S^2}{d_L d_I}} \quad (5)$$

We report both the intercept and the maximum projection sphericity on the smooth surface of grains defined via spherical harmonics.

Roundness

Roundness is a shape characteristic related to the distance traveled by a particle prior to its deposition [14]. Experimental studies indicate that roundness is related to the degree of abrasions and wear suffered by the particle. A qualitative definition of roundness refers to the sharpness of the corners and edges of the grain. However the

main problem in determining the roundness is recognizing the corners. There have been many propositions for an accurate and efficient method to measure roundness [26, 25, 12]. They are based on a visual comparison of individual grains which leads to a number of problems; first the number of grains studied is limited, secondly they are based on 2D projection images and thirdly, it is objective – different operators may estimate different roundness.

We measure the roundness of the particles by deriving the *Maximum Covering Sphere map* [4, 9, 2] for each grain: define locally for every point within the grain, the diameter of the largest sphere which fully lies within the grain and covers that point (Fig. 8). To measure the curvature over the whole grain we find the maximal covering sphere along the surface of the grain and summing over all surface patches derive the average curvature C_{av} for the grain. The roundness of the grain is then defined by $C_{av} \times R$ where R is the maximally inscribed sphere within the grain.

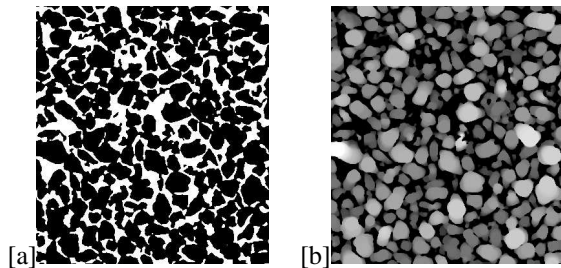


Figure 8: Illustration of the measurement of the roundness of the grains. In [a] a 2D slice of a the poorly consolidated reservoir core is shown with the grains in black. In [b] the corresponding field of maximal covering radii is shown for the granular phase with the gray scale proportional to covering disk radius (brighter indicates larger covering radii).

It is assumed that roundness of rock particles is a property independent of sphericity [24] and it is common to analyse grain shape data via a Sphericity/Roundness plot introduced by Powers [14] (see Fig. 9) and hereafter referred to as a Powers plot.

Shape Class

Other classifications of the shape of grains are used in sedimentology. One common classification is based on the measure of the three primary axes of each grain and gives an indication of the relative length of these axes; from oblate (disk-shaped), equant (sphere or cube-like), to bladed, and prolate (rod-shape). This shape relation is plotted in a diagram commonly called a Zingg diagram [27]. The long, intermediate and small axes of each grain is measured as described previously.

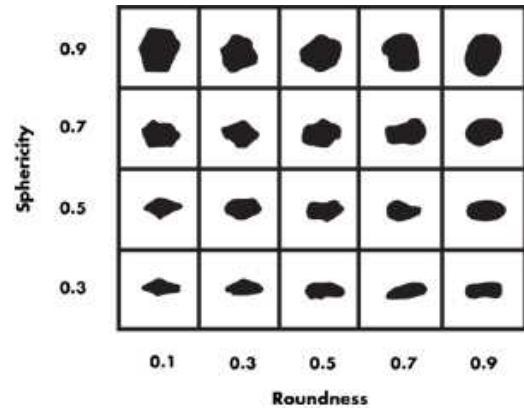


Figure 9: Sphericity/Roundness relationship as given in [14]. Image obtained from <http://www.carboceramics.com/tools/trphysical.html>.

GRAIN FABRIC ANALYSIS

In this section we describe the methodology for obtaining fabric data from the grain images including quantifying the grain packing characteristics (grain to grain contacts, grain overlap area) and orientation.

Grain Connectivity

One of the most important characteristics of packing is the frequency with which grains touch each other. From the grain partitioning algorithm one can immediately identify all grain-to-grain contacts within the full volume. Due to potential biasing at the boundaries we do not consider any grain that is in contact with the edge of the image volume.

Grain Overlap

The total overlap area between grains can also be derived directly from the grain partitioning throughout the full volume. This leads to an estimate of the degree of cementation of the rock. The shape of the grain contact is not ascertained by the algorithm. Due to the nature of the partitioning algorithm, illustrated in Fig. 7, most contacts are long (are approximately planar). Concave/convex and sutured contacts cannot be discerned. The measure of the grain overlap area does allow one to differentiate tangential contacts (small overlap areas) to long contacts.

Grain orientation

From measurement of the three primary axes of the grains one can obtain grain orientation information. We report the orientation of the primary axis d_L of each grain to

describe the degree of preferential orientation within the granular medium.

RESULTS

Here we describe the results for the fabric and texture analysis on the five tomographic samples. The total number of grains imaged in each sample is given in Table 2. The rock and soil samples all include over 4000 imaged grains.

Table 2: Statistics derived from the images of the five samples. We give the number of grains captured per image (No.). We also report the mean volume of the grain, the median grain size, the dispersion (sorting or standard deviation), the skewness and kurtosis of the grain size distribution. All properties are defined in ϕ_g units (Eqn.(1)) and based on the definitions of Folk and Ward [6].

	Foam	Soil1	Soil2	Uncon	PoorSort
No.	1521	5063	5795	8310	4103
ϕ_g	1.74	1.01	1.58	2.70	2.62
Md_{ϕ_g}	1.68	1.10	1.50	2.66	2.69
σ	.37	.35	.52	0.42	1.04
Sk	0.07	-0.07	0.30	0.24	-.45
K	1.09	.97	1.01	1.21	1.30
Z	6.02	5.23	5.63	5.10	7.45

Foam sample

The foam, characterised by reasonably homogeneous spherical pores embedded within a solid matrix and a reasonably narrow distribution of the bubble sizes, is used to validate the fabric analysis algorithms and to give reference values for a homogeneous sphere pack. The analysis is performed on the *pore* phase as this phase mimics a homogeneous spherical grain pack. Data in Table 2 indicates that the system is well sorted, is slightly positively skewed and mesokurtic. In Fig. 10 we summarise the grain size data; the grains are primarily of medium grade with some fine grades ($1 < \phi_g < 3$).

In Fig. 11 we summarise the grain shape data; we find that, as expected, the sphericity and roundness of the 'grains' are both close to 1.0. The data for all grains superimposed on the Power plot shows that all grains lie in the upper right region. The data on the Zingg diagram also lies strongly in the upper right quadrant further underlining the strongly compact spherical shape of the 'grains'. In Fig. 12 and Table 2 we summarise the grain fabric data. The average connectivity of the grains is $\bar{Z} = 6.02$ and

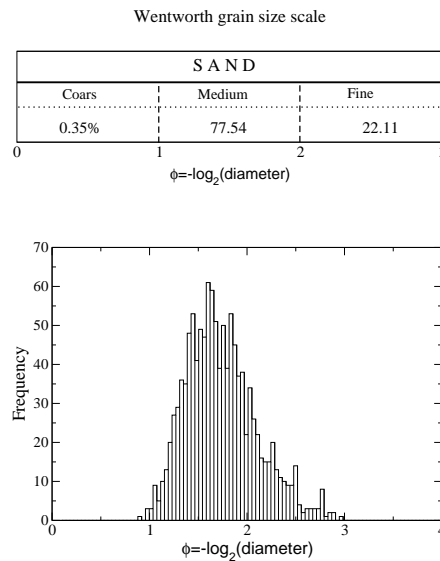


Figure 10: Grain size data for the ideal foam system.

we observe a homogeneous coordination number distribution in Fig. 12(a) with a maximum coordination number of $Z_{max} = 11$. The grain overlap area distribution in Fig. 12(b) is homogeneous with the average overlap area of the order of $.04 \text{ mm}^2$. Despite the homogeneity of the system a very strong anisotropy is observed in the grain orientation (Fig. 12(c)). This is consistent with the manufacturing process which is based on an extrusion process and leads to slight shearing of the system resulting in a small but consistent elongation of the foam structure in one direction.

Soil Sample A

Data in Table 2 is based solely on the statistics measured on the resolved grains which lie within the sand grade scales (very coarse \rightarrow very fine). The results indicate that the first soil system is well to very well sorted, is near symmetrical and mesokurtic. In Fig. 13 we summarise the grain size data; the grains are primarily of coarse and medium grade ($0 < \phi_g < 2$).

In Fig. 14 we plot data from a laser particle size experiment on a sister core of the soil sample. The particle size data shows a bimodal distribution with a significant fraction (29.1%) of the grains lying in the silt/clay range and most of the remaining grains within the coarse to medium sand grades. The binarization of this core (recall Table 1) led to an estimate of the intermediate phase volume (clay/silt fraction) as 34% in reasonable agreement with the particle size data. We compare the histogram

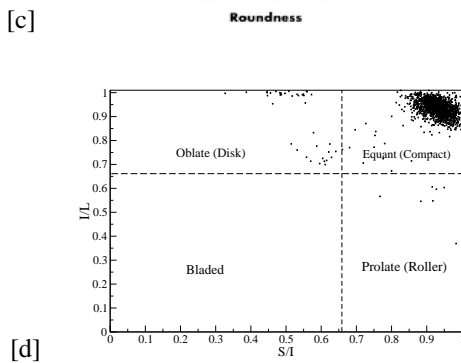
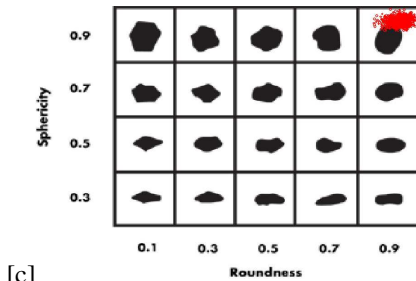
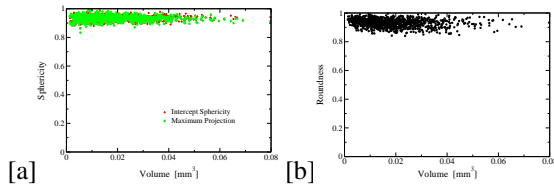


Figure 11: Grain shape data for the ideal foam system. (a) Sphericity and (b) roundness are plotted as a function of grain volume. (c) Sphericity/roundedness and (d) Zingg diagram for the system.

from the digital image data to the data from the particle size analysis for the sand fraction in Fig. 13(b). The agreement is good.

In Fig. 15 we summarise the grain shape data. The Sphericity data lies between values of 0.4 and 0.7 with a slight bias to larger sphericity for larger grains. The roundness data lies in the rounded to well rounded range with larger values observed for smaller grains. The data for all grains superimposed on the Powers plot shows a spread of grain shape across the sample. The data on the Zingg diagram also varies over a wide range indicating the breadth of grain shapes measured on this sample.

In Fig. 16 and Table 2 we summarise the grain fabric data. The average connectivity of the grains is $\bar{Z} = 5.23$ and we observe a broader coordination number distribution in Fig. 16(a). No grains of $Z < 3$ are noted as expected since a stable packing for any grain would initially have a minimum of 3 neighbours. The peak in the distribution lies at a coordination number of $Z = 3$ and more than 50% of the grains have a $Z \leq 4$. $Z = 3$ corre-

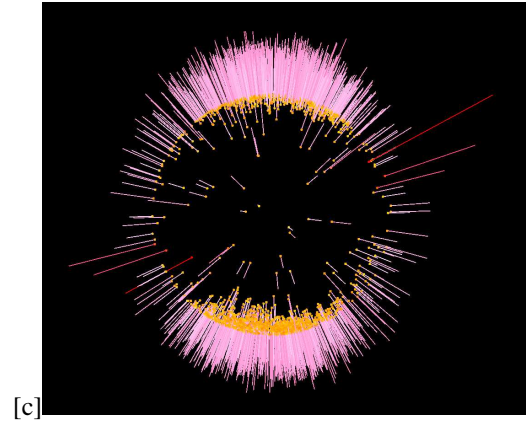
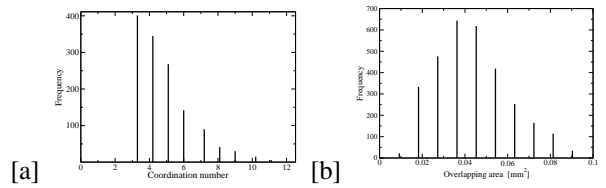


Figure 12: Grain fabric data for the homogeneous foam; (a) coordination number distribution and (b) overlap area distribution. In (c) the orientation of the longest axis is shown along a hemisphere— there is a strong preference for a single direction. The direction of the elongated axis is shown for each grain and the length of the lines is proportional to the equivalent radius of the grain.

sponds to a loose grain and $Z = 4$ is the minimum coordination number in 3D for a grain to be stable. The large number of grains of low coordination indicates that many grains may be loose within the pack and may indicate that the pack is weakly grain supported or matrix supported. We also note that a small number of grains exhibit very high coordination. In Fig. 16(b) we plot the coordination number versus grain volume. We note that the grains of high coordination correspond to the grains of largest volume as expected. In Fig. 17 we show two snapshots from a rendered 3D movie of a highly coordinated ($Z = 22$) grain showing that many smaller grains are attached to this large grain. The grain overlap area distribution in Fig. 16(c) is positively skewed with the mean overlap area of the order of $.4 \text{ mm}^2$. No anisotropy in the grain orientation is observed in Fig. 16(d)— the direction of the longest axis seems equally weighted along all orientations.

Soil Sample B

In contrast to Soil A, data in Table 2 indicates that the second soil system is only moderately sorted, is strongly positively skewed and mesokurtic. This highlights the

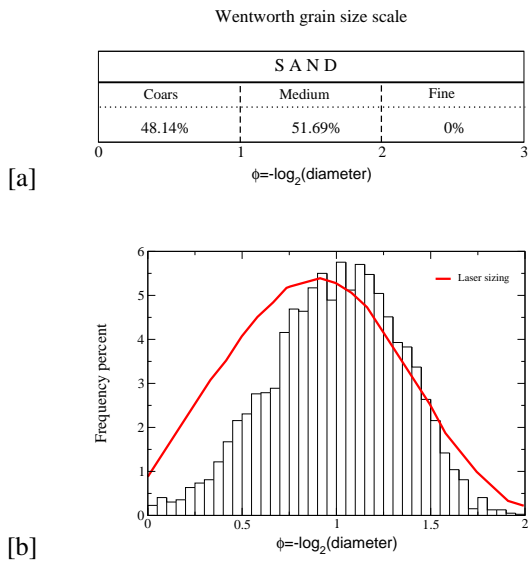


Figure 13: Grain size data for the first soil sample. In (b) we also show the grain size distribution for the sand fraction obtained by laser particle sizing (Fig. 14 on a sister plug). The agreement is excellent.

heterogeneity in this soil despite the proximity of the two samples. In Fig. 18 we summarise the grain size data; the grains are primarily of medium grade with some coarse and fine fractions ($0 < \phi_g < 3$). A small amount of very fine/silt fraction ($\phi_g = 4 - 6$) is also observed. We again can compare this analysis to the data from laser particle sizing on a sister core by overlaying the histogram from the digital data onto the data from the particle size anal-

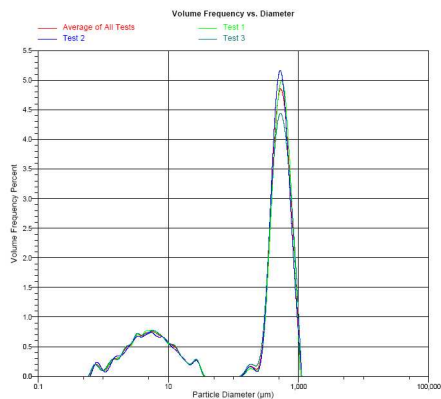


Figure 14: Grain size data for soil sample obtained by laser particle sizing.

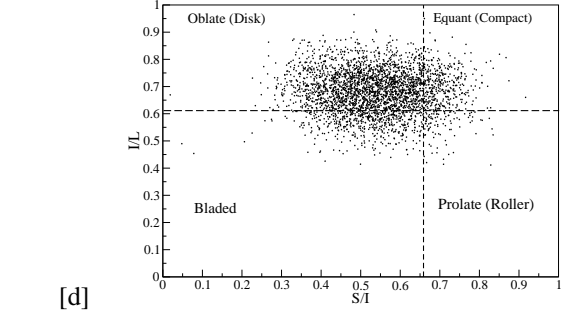
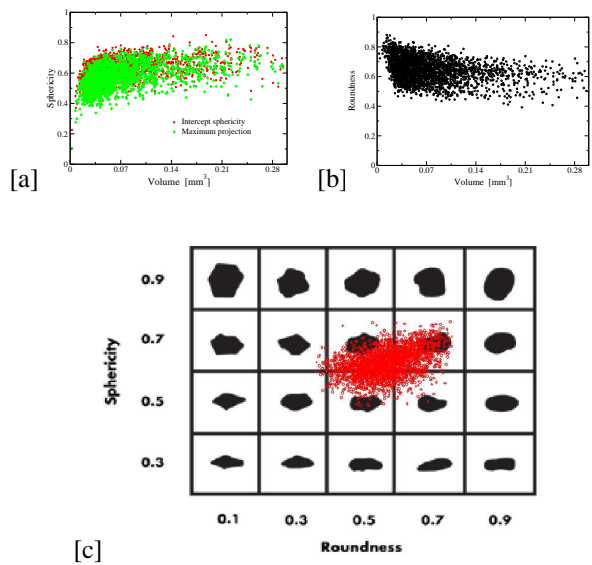


Figure 15: Grain shape data for the first soil sample. Arrangement as in Fig. 11.

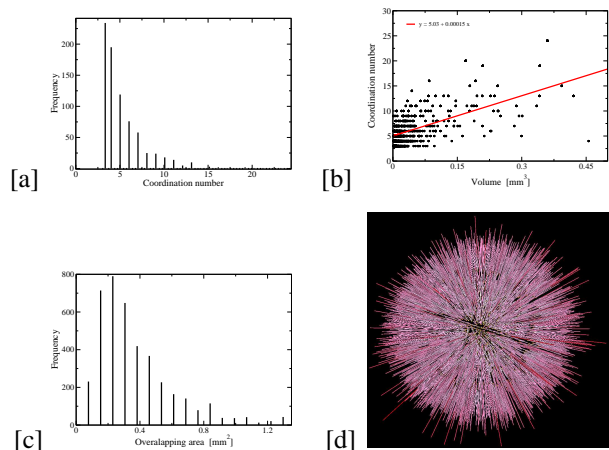


Figure 16: Grain fabric data for soil A sample.

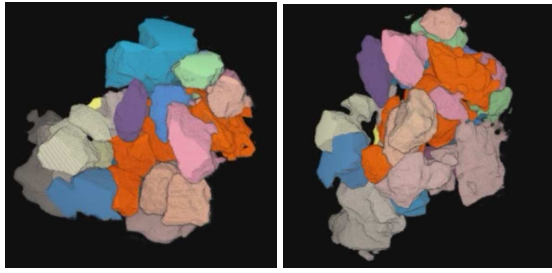


Figure 17: Two images of a highly coordinated grain (orange) and its neighbouring grains from a rendered 3D movie.

ysis for the sand fraction in Fig. 18(a). The digital data is now biased to lower grain sizes compared to both the Soil A sample and the laser data. This again highlights the heterogeneity in grain sizes within this soil.

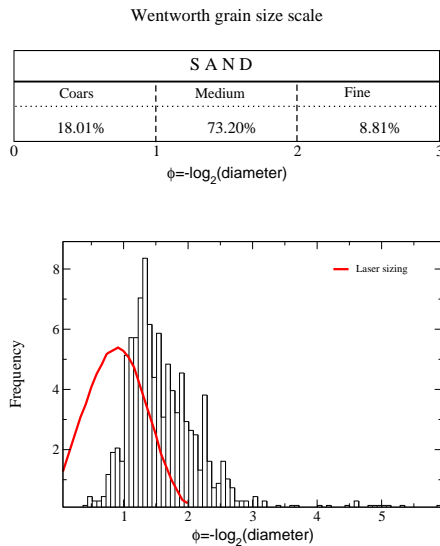


Figure 18: Grain size data for the second soil sample.

In Fig. 19 we summarise the grain shape data. Similar to the data for Soil A (recall Fig. 15), sphericity data lies between values of 0.4 and 0.7 with a very slight bias to larger sphericity for larger grains. The roundness data lies in the rounded to well rounded range with larger values observed for smaller grains. The data for all grains superimposed on the Power plot shows a similar spread of grain shape across the sample. The data on the Zingg diagram also varies over a wide range indicating the breadth of grain shapes measured on this sample. In Fig. 20 and Table 2 we summarise the grain fabric data. The average connectivity of the grains is $\bar{Z} =$

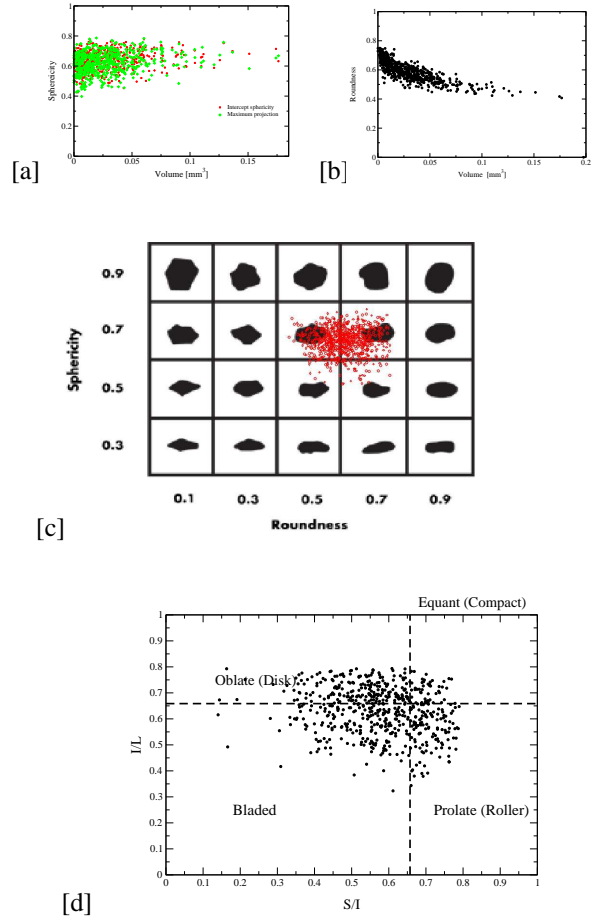


Figure 19: Grain shape data for the second soil sample. Arrangement as in Fig. 11.

5.63 and we observe a slightly broader coordination number distribution in Fig. 20(a) than in Fig. 16(a). The peak in the distribution lies at a coordination number of $Z = 3$ and $Z = 4$ again indicating that a large number of grains are loose or potentially loose within the pack. The grain overlap distribution in Fig. 20(b) is positively skewed with the mean overlap area of the order of $.4 \text{ mm}^2$. No anisotropy in grain orientation is observed (Fig. 20(c)).

Unconsolidated Reservoir Core

Data in Table 2 indicates that the unconsolidated reservoir sand is well sorted, exhibits slight positive skewness and is platykurtic. In Fig. 21 we summarise the grain size data; the resolved grains are primarily of a fine to very fine grade ($2 < \phi_g < 4$). No experimental laser particle sizing data was available for this core.

In Fig. 22 we summarise the grain shape data. The Sphericity data lies between values of 0.7 and 0.9. The roundness

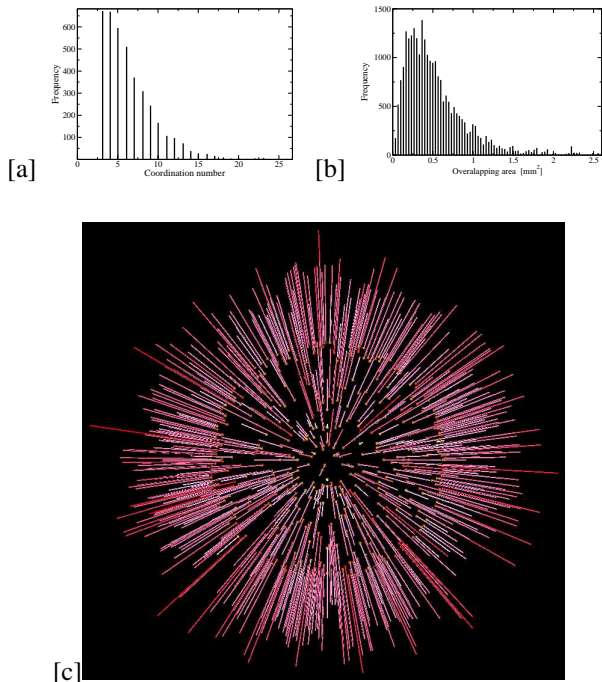


Figure 20: Grain fabric data for soil B sample.

data lies primarily between 0.4 and 0.6 (rounded grains) and shows a bias to larger values observed for smaller grains. The data for all grains superimposed on the Power plot shows a similar grain shape within the sample. The data on the Zingg diagram lies primarily in the compact

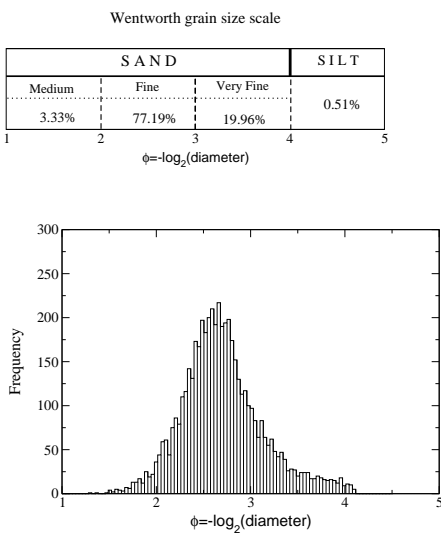


Figure 21: Grain size data for the unconsolidated reservoir core sample.

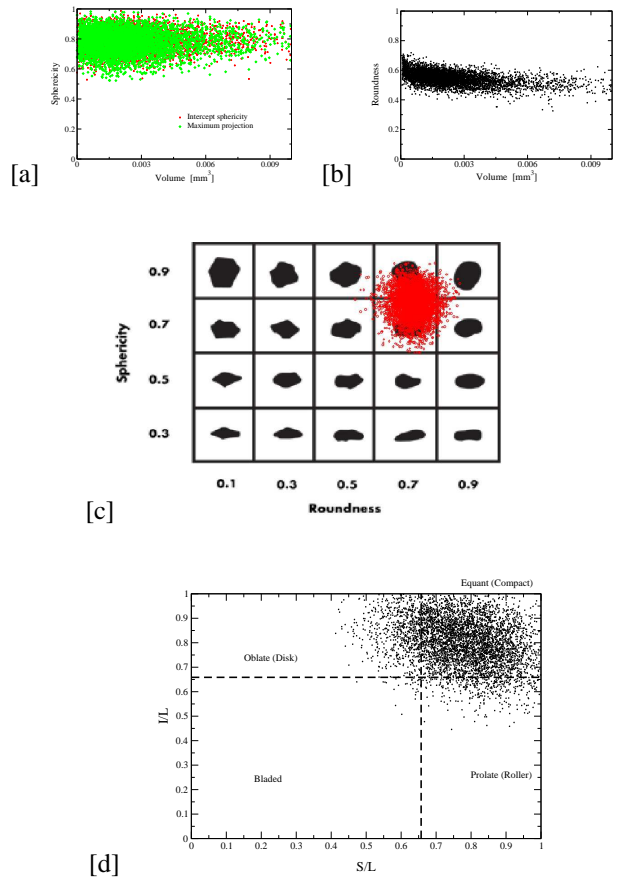


Figure 22: Grain shape data for the unconsolidated reservoir core sample. Arrangement as in Fig. 11.

quadrant.

In Fig. 23 and Table 2 we summarise the grain fabric data. The average connectivity of the grains is $\bar{Z} = 5.10$ and we observe a broad coordination number distribution in Fig. 23(a). This low $\bar{Z} = 5.10$ may indicate the looseness of the packing despite the high grain volume fraction. Also the peak in the distribution lies at a coordination number of $Z = 3, 4$ indicating that a large number of grains are loose within the pack. The grain overlap distribution in Fig. 23(b) is narrow and positively skewed with the mean overlap area of the order of $.04 \text{ mm}^2$. No anisotropy in grain orientation is observed (Fig. 23(c)).

Poorly Sorted Core

Data in Table 2 indicates that the unconsolidated reservoir sand is very poorly sorted $\sigma = 1.04$, is strongly negatively skewed and very platykurtic. In Fig. 24 we summarise the grain size data; the resolved grains vary from very coarse to a very fine grade ($-1 < \phi_g < 4$). Again no laser particle sizing data was available for direct comparison.

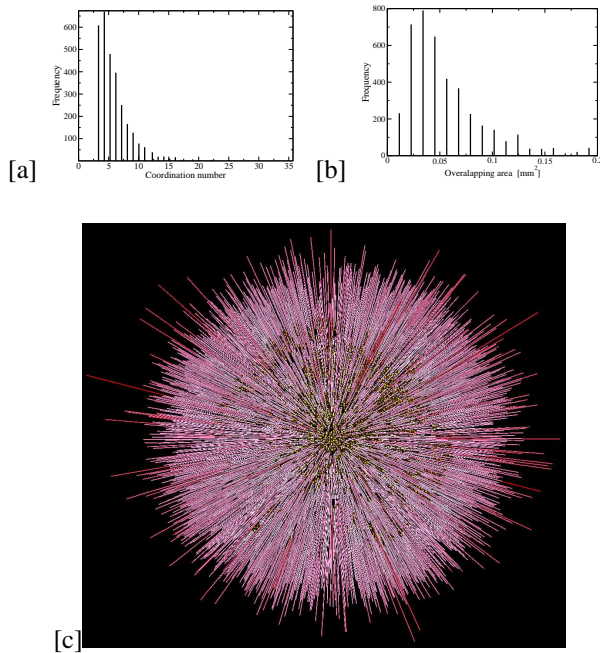


Figure 23: Grain fabric data for the unconsolidated reservoir core sample.

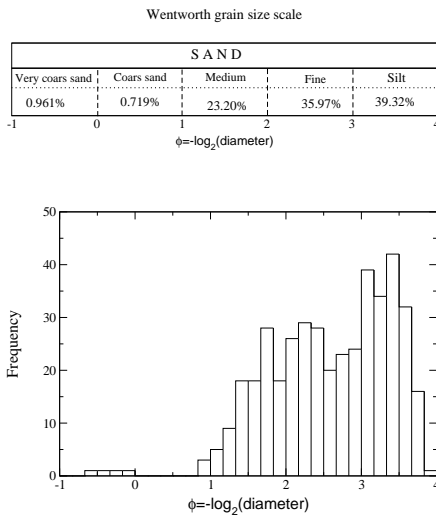


Figure 24: Grain size data for the poorly sorted reservoir core sample.

In Fig. 25 we summarise the grain shape data. The grains are not spherical with sphericity values of 0.4 to 0.7. The roundness data lies primarily between 0.5 and 0.9 (rounded to well rounded grains) and as seen previously, shows a bias to larger values for smaller grains. The data for all grains superimposed on the Power plot shows a broad distribution of grain shape within the sample. The data on the Zingg diagram lies primarily in the prolate quadrant.

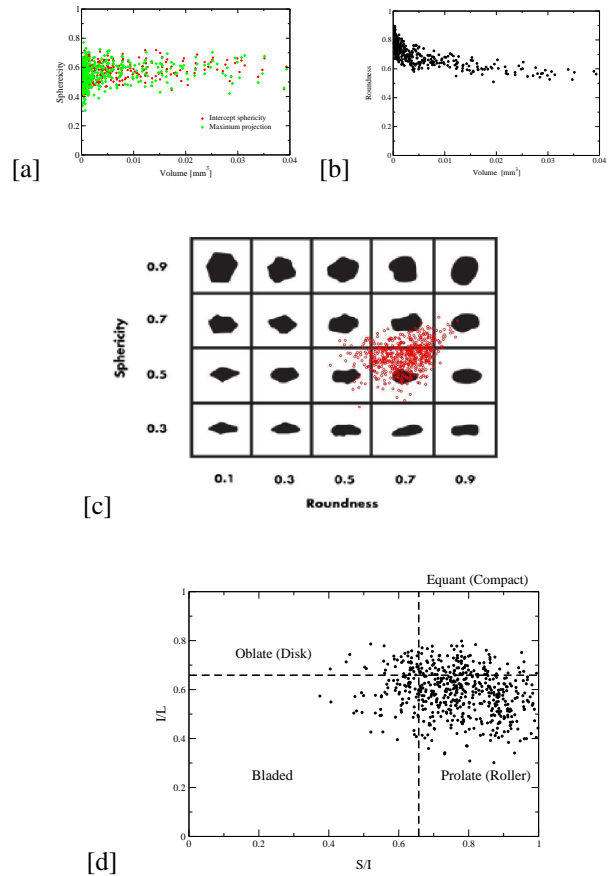


Figure 25: Grain shape data for the poorly sorted reservoir core sample. Arrangement as in Fig. 11.

In Fig. 26 and Table 2 we summarise the grain fabric data. The average connectivity of the grains is $\bar{Z} = 7.24$ and we observe a very broad coordination number distribution in Fig. 26(a). Again, the peak in the distribution lies at a coordination number of $Z = 3$ but one also observed some grains (largest) with coordination numbers of $Z \geq 60$. The grain overlap distribution in Fig. 26(b) is broad, strongly skewed with the mean overlap area per grain of the order of $.3 \text{ mm}^2$. We observe some anisotropy in the grain orientation in Fig. 26(c). It is not clear if the axis corresponding to the preferential alignment of the grains is along the bedding plane of the core.

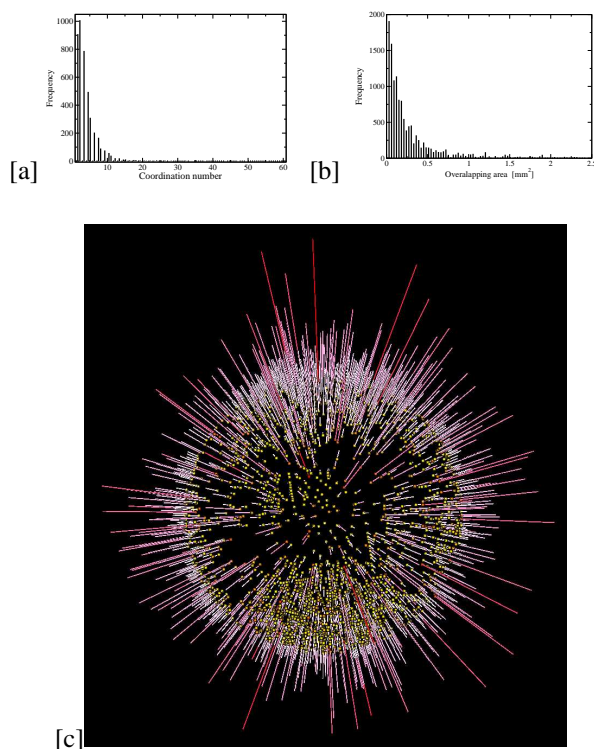


Figure 26: Grain fabric data for poorly sorted sample.

CONCLUSIONS

1. We demonstrate the ability to directly measure rock fabric and texture from 3D digital images of rock fragments. We describe two methods to distinguish individual grains from a complex image. We then describe methods for the characterisation of individual grains including grain size data (max/min, mean, median, mode, skewness, sorting and kurtosis), grain shape data (sphericity, roundness) and textural information (sorting, grain contacts, matrix/grain supported). Current measures of grain size and shape are often based on visual comparisons for 2D projections and are subject to operator bias. The rock fabric and textural data obtained from 3D images is more comprehensive, systematic and quantitative than current analysis techniques.
2. We characterise five individual samples including a model foam and 4 sedimentary samples. The samples encompass a broad spectrum of grain fabric and texture. The resultant analysis on up to 8000 grains per image gives a wide distribution of grain size and sorting values. Grain size data based on the Wentworth scale are analysed from very fine sands/silts through to very coarse sands. Compar-

ison of grain size data from the digital method to data from laser particle sizing on a sister core sample is consistent.

3. Grain shape data varies considerably across samples. The model homogeneous system is very strongly rounded and spherical. The sedimentary systems vary from subrounded to well rounded and have sphericity values from 0.3 – 0.9. Systematic variations in grain shape are noted with grain size. A plot of the roundness and sphericity for all grains within a sample allows one to gauge mean particle shape as well as the spreads in the measures.
4. Grain fabric data varies with sorting and consolidation. The three poorly consolidated sedimentary systems all have mean connectivity of $5.1 < Z < 5.6$. In contrast the more cemented and poorly sorted sand exhibits a higher connectivity $Z = 7.45$. All samples exhibit a large number of grains with coordination number of $Z = 3$ which corresponds to a loose grain. Grain overlap areas are measured and may be linked to the degree of cementation of a rock.

ACKNOWLEDGEMENTS

The authors acknowledge the Australian Government for their support through the ARC grant scheme. We also thank the CRC for FCS, CRC LEME, BHP-Billiton Petroleum and Woodside Energy who have provided core material for this study and financial support for the facility. We thank the A.N.U. Supercomputing Facility and the Australian Partnership for Advanced Computing for very generous allocations of computer time. We thank Wayne Alger and Chris Cubitt from Woodside Energy for comments on the submission and MS thanks Dr. E. Garboczi of NIST for discussions and assistance with the spherical harmonics calculations.

REFERENCES CITED

[1] Arns, C. H., A. Sakellariou, T. J. Senden, A. P. Sheppard, R. M. Sok, W. V. Pinczewski, and M. A. Knackstedt: 2004, 'Digital Core Laboratory: Reservoir core analysis from 3D images'. In: *Presented at the SPWLA Annual Logging Symposium*. Noordwijk.

[2] Arns, C. H., A. Sakellariou, T. J. Senden, A. P. Sheppard, R. M. Sok, W. V. Pinczewski, and M. A. Knackstedt: 2005, 'Digital Core Laboratory: Reservoir core analysis from 3D images'. *Petrophysics* **46** (3), to appear, May 2005.

- [3] Caselles, V., R. Kimmel, and G. Shapiro: 1997, 'Geodesic active contours'. *Int. J. Comput. Vis.* **22**, 61–79.
- [4] Coles, M. E., R. D. Hazlett, E. L. Muegge, K. W. Jones, B. Andrews, B. Dowd, P. Siddons, A. Peshkin, P. Spanne, and W. E. Soll: 1998, 'Developments in Synchrotron x-ray microtomography with applications to flow in porous media'. *SPE Reservoir Evaluation and Engineering* **36531**, 288–296.
- [5] Duncan, B. and D. Olson: 1993, 'Approximation and characterization of molecular surfaces'. *Biopolymers* **33**, 219–229.
- [6] Folk, R. L. and W. C. Ward: 1957, 'Brazos River Bar: A study in the significance of grain size parameters'. *J. Sedimentary Petrology* **27**, 3–27.
- [7] Fujimoto, R. M.: 1999, *Parallel and distributed simulation systems*. Wiley-Interscience.
- [8] Garboczi, E. J.: 2002, 'Three dimensional mathematical analysis of particle shape using x-ray tomography and spherical harmonics: Applications to aggregates used in concrete'. *Cement and Concrete Research* **32**, 1621–1638.
- [9] Hilpert, M. and C. T. Miller: 2001, 'Pore-morphology based simulation of drainage in totally wetting porous media'. *Advances in Water Resources* **24**, 243–255.
- [10] Knackstedt, M. A., C. H. Arns, A. Sakellariou, T. J. Senden, A. P. Sheppard, R. M. Sok, W. V. Pinczewski, and G. F. Bunn: 2004, 'Digital Core Laboratory: Properties of Reservoir Core derived from 3D images'. In: *Presented at the Asia-Pacific Conference on Integrated Modelling for Asset Management*. Kuala Lumpur.
- [11] Krumbein, W. C.: 1934, 'Size frequency distributions of sediments'. *J. Sedimentary Petrology* **4**, 65–77.
- [12] Krumbein, W. C.: 1941, 'Measurement and geological significance of shape and roundness of sedimentary particles'. *J. Sed. Petrol.* **11**, 67–76.
- [13] Perona, P. and J. Malik: 1990, 'Scale-space and edge-detection using anisotropic diffusion'. *IEEE Trans. Pattern Anal. Mach. Intell.* **12**, 629–639.
- [14] Powers, M. C.: 1953, 'A new roundness scale for sedimentary particles'. *J. Sedimentary Petrology* **23**, 117–119.
- [15] Pratt, W. K.: 2nd Ed, 1991, *Digital Image Processing*. John Wiley and Sons, New York.
- [16] Press, W. H., B. P. Flannery, S. A. Teukolsky, and W. T. Vetterling: 1992, *Numerical Recipes: The Art of Scientific Computing*. Cambridge: Cambridge University Press.
- [17] Sakellariou, A., C. H. Arns, A. Limaye, T. J. Senden, A. P. Sheppard, R. M. Sok, W. V. Pinczewski, M. A. Knackstedt, L. Berge, and P. Øren: 2003, 'μ-CT facility for imaging reservoir rocks at pore scales'. In: *SEG Technical Program*. Dallas, Texas.
- [18] Sakellariou, A., T. J. Sawkins, T. J. Senden, and A. Limaye: 2004a, 'X-ray tomography for mesoscale physics applications'. *Physica A* **339**, 152–158.
- [19] Sakellariou, A., T. J. Senden, T. J. Sawkins, M. A. Knackstedt, A. Limaye, C. H. Arns, A. P. Sheppard, and R. M. Sok: 2004b, 'An x-ray tomography facility for a wide range of mesoscale physics applications'. In: U. Bonse (ed.): *Proceedings of SPIE*, Vol. 5535. Bellingham, WA, pp. 166–171.
- [20] Sheppard, A. P., R. M. Sok, and H. Averdunk: 2004, 'Techniques for Image Enhancement and Segmentation of Tomographic Images of Porous Materials'. *Physica A* **339**, 145–151.
- [21] Sneed, E. D. and R. L. Folk: 1958, 'Pebbles in the lower Colorado river, Texas; a study in particle morphogenesis'. *Jour. Geol.* **66**, 114–150.
- [22] Soille, P.: 2nd Ed, 2003, *Morphological Image Analysis: Principles and Applications*. Springer-Verlag.
- [23] Vincent, L. and P. Soille: 1991, 'Watersheds in digital spaces— an efficient algorithm based on immersion'. *IEEE Trans. Pattern Anal. Machine Intell.* **13**, 583–598.
- [24] Wadell, H.: 1932, 'Volume, shape and roundness of rock particles'. *Jour. Geol.* **40**, 443–451.
- [25] Wadell, H.: 1935, 'Volume, shape and roundness of quartz particles'. *Jour. Geol.* **43**, 250–261.
- [26] Wentworth, C. K.: 1919, 'A laboratory and field study of cobble abrasion'. *Jour. Geol.* **27**, 507–521.
- [27] Zingg, T.: 1935, 'Beitrage zur Schotteranalyse'. *Schweiz. min. pet. Mitt.* **15**, 39–140.
- [28] Zuber, M. T., D. Smith, A. Cheng, J. Garvin, O. Aharonson, and T. Cole: 2000, 'The shape of 433 eros from the near-shoemaker laser rangefinder'. *Science* **289**, 1788–1793.

ABOUT THE AUTHORS

M. Saadatfar: was awarded a BSc from the Institute of Advanced Studies in Zanjan Iran and is an ANU PhD candidate.

M. L. Turner: was awarded a BSc (Hons) in Geology from ANU and is now an ANU PhD candidate.

C. H. Arns: Christoph Arns was awarded a Diploma in Physics (1996) from the University of Technology Aachen and a PhD in Petroleum Engineering from the University of New South Wales in 2002. He is a Research Fellow at the Department of Applied Mathematics at the Australian National University. His research interests include the morphological analysis of porous complex media from 3D images and numerical calculation of transport and linear elastic properties with a current focus on NMR responses and dispersive flow. Member: AMPERE, ANZMAG, ARMA, DGG.

H. Averdunk: Holger Averdunk has studied Molecular Biology and Computer Science. He has worked in Bioinformatics and the IT Industry. Currently he is working on 3D filters and Segmentation methods.

T.J. Senden: Timothy John Senden received his training and PhD in physical chemistry at the Australian National University in 1994. His principal techniques are atomic force microscopy and surface force measurement, but more recently micro-X-ray tomography. His research centres around the application of interfacial science to problems in porous media, granular materials, polymer adsorption and single molecule interactions.

A.P. Sheppard: Adrian Sheppard received his B.Sc. from the University of Adelaide in 1992 and his PhD in 1996 from the Australian National University and is currently a Research Fellow in the Department of Applied Mathematics at the Australian National University. His research interests are network modelling of multiphase fluid flow in porous material, topological analysis of complex structures, and tomographic image processing.

R. M. Sok: Rob Sok studied chemistry and received his PhD (1994) at the University of Groningen in the Netherlands and is currently a Research Fellow in the Department of Applied Mathematics at the Australian National University. His main areas of interest are computational chemistry and structural analysis of porous materials.

W. V. Pinczewski: W.V Pinczewski holds BE (Chem.Eng) and PhD degrees from the University of New South Wales (UNSW). He is Head of the School of Petroleum En-

gineering at UNSW. His research interests include improved oil recovery, multi-phase flow and transport properties in porous media and network modelling.

J. Kelly: J.C. Kelly holds BSc Hons (Geology) and PhD degrees from La Trobe University and is currently a Senior Petrophysicist with Woodside Energy. His main areas of interest are formation evaluation and reservoir characterisation.

M.A. Knackstedt: Mark Knackstedt was awarded a BSc in 1985 from Columbia University and a PhD in Chemical Engineering from Rice University in 1990. He is an Associate Professor at the Department of Applied Mathematics at the Australian National University and a Visiting Professor at the School of Petroleum Engineering at the University of NSW. His work has focussed on the characterisation and realistic modelling of disordered materials. His primary interests lie in modelling transport, elastic and multi-phase flow properties and development of 3D tomographic image analysis for complex materials.